Electrochimica Acta 97 (2013) 42–51

Contents lists available at SciVerse ScienceDirect

Electrochimica Acta

journal homepage: www.elsevier.com/locate/electacta

Investigations of lithium–sulfur batteries using electrochemical impedance spectroscopy

Natalia A. Cañas[a,b,*], Kei Hirose[a], Brigitta Pascucci[a,c], Norbert Wagner[a,1], K. Andreas Friedrich[a,b], Renate Hiesgen[c]

[a] Institute of Technical Thermodynamics, German Aerospace Center, Stuttgart, Germany
[b] Institute for Thermodynamic and Thermal Engineering, University of Stuttgart, Germany
[c] Faculty of Basic Science, University of Applied Sciences Esslingen, Esslingen, Germany

ARTICLE INFO

Article history:
Received 10 December 2012
Received in revised form 15 February 2013
Accepted 20 February 2013
Available online 1 March 2013

Keywords:
Lithium–sulfur battery
Electrochemical impedance spectroscopy
Degradation

ABSTRACT

The electrochemical behavior of lithium–sulfur (Li–S) batteries was investigated by means of electrochemical impedance spectroscopy (EIS). Measurements were performed in equidistant charge intervals at different depths of discharge and charge during the first cycle. Additionally, the degradation of the cells was analyzed for up to 50 cycles. An equivalent electrical circuit is proposed to simulate the electrochemical processes and to quantify the impedance contributions of Li–S batteries. EIS as a function of the cycle number shows an increased capacity for fading correlated with a decrease in the charge transfer resistance of the cathode. Atomic force microscopy (AFM) was also used to provide information about changes in the electrical conductivity of the cathode surface as they are related to the building of isolating films.

1. Introduction

Over the last few decades, studies of new secondary cells have increased considerably. This increase is due to a demand for high energy density rechargeable batteries for various applications such as consumer electronics and electro-mobility. The Li–S battery is a promising system due to its high theoretical capacity (1675 mAh g_{sulfur}^{-1}), energy density (2500 Wh kg^{-1}), low cost and the non-toxicity of sulfur. Nevertheless, some of the drawbacks of Li–S batteries include their poor rechargeability and high self-discharge rates. Due to the low electrical conductivity of sulfur, electrically conductive material must be added to encourage an electrochemical reaction. Furthermore, polysulfides of high orders (Li_2S_n with $2 \leq n \leq 8$) dissolve in the electrolyte and can diffuse to the anode and react directly with lithium metal. This so-called shuttle mechanism causes the irreversible loss of sulfur [1–3]. Insulating and insoluble polysulfide discharge product (Li_2S) can also precipitate on the surface of electrodes, preventing further electrochemical reactions.

EIS is a powerful technique used to investigate the physical and electrochemical processes occurring in batteries during charge and discharge. This method is used in the characterization of Li–S batteries to study, amongst other topics, the influence of electrode protective layers [4–6], cathode materials [7–13] and electrolyte compositions [14–18] in the impedance of the cell. Few studies have applied EIS at different depths of charge or discharge [19–22]. In these studies, such measurements were performed using potentiostatic mode with an amplitude signal of 5 mV at different frequency ranges (100 kHz–100 mHz [19], 1 MHz–10 mHz [20], 65 kHz–1 Hz [21], 200 kHz–1 mHz [22]).

The processes described by the proposed equivalent circuits (ECs) in [19] are electrolyte resistance (R_e), the formation of the conductive agent/electrolyte interface (Rct//CPE_1), Li_2S film formation (Rg//CPE_2) and polysulfide diffusion (Warburg element, W_0). The element R//CPE is defined as a resistance (R) connected in parallel to a constant phase element (CPE). Similar ECs were applied for the fitting of the impedance spectra in [21]. The processes analyzed here were electrolyte resistance (R_{el}), surface layer formation on lithium and sulfur electrodes (R_1//CPE_1), the electrochemical reaction of sulfur (Rr//CPE_r) and polysulfide diffusion (W).

In a recent study [22], spectra obtained at high frequencies were not analyzed, and therefore, no electrolyte resistance was considered. The boundary electrode/electrolyte was also described by a Rct//CPE_{dl} element, new phase formation was represented by a Rct//CPE_f element, and the liquid-state diffusion of soluble polysulfides was defined by a CPE_1 rather than a Warburg element.

* Corresponding author at: Institute of Technical Thermodynamics, German Aerospace Center, Stuttgart, Germany. Tel.: +49 711 6862 576; fax: +49 0711 6862 474.
E-mail addresses: natalia.canas@dlr.de, nataliacanas@gmail.com (N.A. Cañas).
[1] Electrochemical Society Active Member.

0013-4686/$ – see front matter © 2013 Elsevier Ltd. All rights reserved.
http://dx.doi.org/10.1016/j.electacta.2013.02.101

The models used in these studies can fit impedance spectra at high or low frequency regions. In this paper, changes in the impedance of Li–S batteries were studied by means of EIS at different depths of discharge/charge over a wide frequency range. We proposed a simple but consistent EC to quantify the impedance contributions related to each physical or electrochemical process occurring in the battery. Moreover, the impedance spectra of Li–S batteries were evaluated in discharge and charge states for up to 50 cycles. AFM measurements on the cathode provided additional information about the electrical conductivity of the cathode surface, confirming the formation of a non-conductive layer after cycling.

2. Experimental procedures

2.1. Cell preparation

The cathodes used consisted of 50 wt.% sulfur (99.5%, Alfa Aesar), 40 wt.% Super P conductive carbon black (99%, Alfa Aesar) and 10 wt.% polyvinylidene fluoride (PVDF, Alfa Aesar). The cathodes were prepared according to methods previously published [23].

The battery was built in what is known as a Swagelok cell (Fig. 1) and assembled in a glove box under an argon atmosphere. First, a cathode was placed on an aluminum disk over the spring (cathode collector). The separator, a 25 μm thick polypropylene microporous membrane (Celgard 2500), was placed on top of the anode and soaked with 14 μL electrolyte, 1 M $LiPF_6$ (99.99%, Sigma–Aldrich) in tetraethylene glycol dimethyl ether (99.9%, Sigma–Aldrich). Next, a 1.5 mm thick lithium anode (99.9%, Sigma–Aldrich) was placed on the separator. To complete construction of the battery, the cell was tightened until there was no gap between the nut and body hexes. To avoid a short circuit, the diameters of the lithium foil and cathode were 10 mm, while the separator diameter was 2 mm larger.

2.2. Electrochemical impedance spectroscopy and cycling of the battery

The cycling performance of the battery was investigated using a Zahner® IM6 electrochemical workstation with Thales battery software (Zahner®). The charge–discharge procedure was performed galvanostatically at a current density of 300 mA g_{sulfur}^{-1} in a voltage range of 2.8–1.5 V. After reaching the charge end voltage of 2.8 V, a potentiostatic period occurred for 15 min before the next cycle began.

EIS measurements were performed at the same electrochemical workstation during cycling in equidistant charge intervals of 50 mC. Each spectrum was measured in the frequency range of 1 MHz to 60 mHz and with an excitation voltage of 5 mV. The experimental data were fitted with an EC created with Thales software.

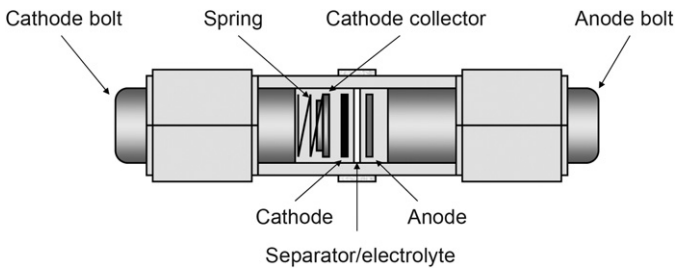

Fig. 1. Scheme of the Swagelok®-cell with an inside view of the battery components.

2.3. Atomic force microscopy

The electrical behavior of the cathode was investigated ex situ by means of an atomic force microscope (Multimode 8, Bruker Corp.). Each tip-sample interaction was analyzed with PeakForce-TUNA™ mode. The current was measured with a Pt-coated conductive tip working in tapping mode at a 1 kHz frequency and with a scan rate of 0.5 Hz. A voltage (100 mV) was applied between the tip and the sample holder and the averaged steady state current was measured at each tip-surface contact. The samples were analyzed in three different positions on the cathode surface and scanned over a 9 μm^2 area. More detailed information about the experimental work performed with AFM can be found in [24].

3. Results and discussion

3.1. EIS measurements during cycling

The electrochemical reaction steps occurring during discharging are described by the reactions (1)–(9). At the anode surface, lithium oxidizes to Li^+ in accordance with reaction (1). In the cathode, sulfur first dissolves into the electrolyte (reaction (2)) and then reduces to polysulfides S_x^{-2}, where $x = 8–1$ (reactions (3)–(8)). Only the formation of solid Li_2S has been experimentally detected; for this reason, the precipitation reaction at the end of the discharge is only presented for this polysulfide (9). During charging, a reversible route is expected. This reaction mechanism is simplified, as the dissociation of polysulfides has not been described. The complete proposed sulfur reduction mechanism is discussed in [25]; the authors describe not only the irreversible electrochemical reaction but also the disproportionation of polysulfides in the electrolyte.

$$Li \rightarrow Li^+ + e^- \quad (1)$$

$$S_{8(s)} \rightarrow S_{8(diss)} \quad (2)$$

$$1/2S_{8(l)} + e^- \rightarrow 1/2S_8^{-2} \quad (3)$$

$$3/2S_8^{-2} + e^- \rightarrow 2S_6^{-2} \quad (4)$$

$$S_6^{-2} + e^- \rightarrow 3/2S_4^{-2} \quad (5)$$

$$3/2S_4^{-2} + e^- \rightarrow 2S_3^{-2} \quad (6)$$

$$S_3^{-2} + e^- \rightarrow 3/2S_2^{-2} \quad (7)$$

$$1/2S_{2(l)}^{-2} + e^- \rightarrow S_{(l)}^{-2} \quad (8)$$

$$2Li^{+1} + S_{(l)}^{-2} \rightarrow Li_2S_{(s)}\downarrow \quad (9)$$

Although these reactions run in parallel during discharge, the electrochemistry of the cell may be divided into three distinct periods according to the state of aggregation of the reactants and products, as follows: (a) solid state → dissolved in electrolyte, (b) dissolved in electrolyte → dissolved in electrolyte and (c) dissolved in electrolyte → solid state. During charge, Li_2S reacts reversibly to S_8. Due to the modification of the aggregate state of the reacting components, significant changes in the impedance contributions related to these processes are expected. The end products of the discharge and charge, in the case of a complete reaction, are non-conductive solid materials; this can influence the charge transfer resistance in the electrodes and enhance the formation of isolating surface layers.

Figs. 2(a) and 3(a) show the first discharge and charge curves of the Li–S battery and the points at which EIS spectra were recorded. For clarity, only certain spectra are shown (Figs. 2(b–e) and 3(b–e)). The frequency-dependent impedance of the cell represents the response of several parallel processes occurring in the battery. The impedance plots measured during cycling reveal these processes in

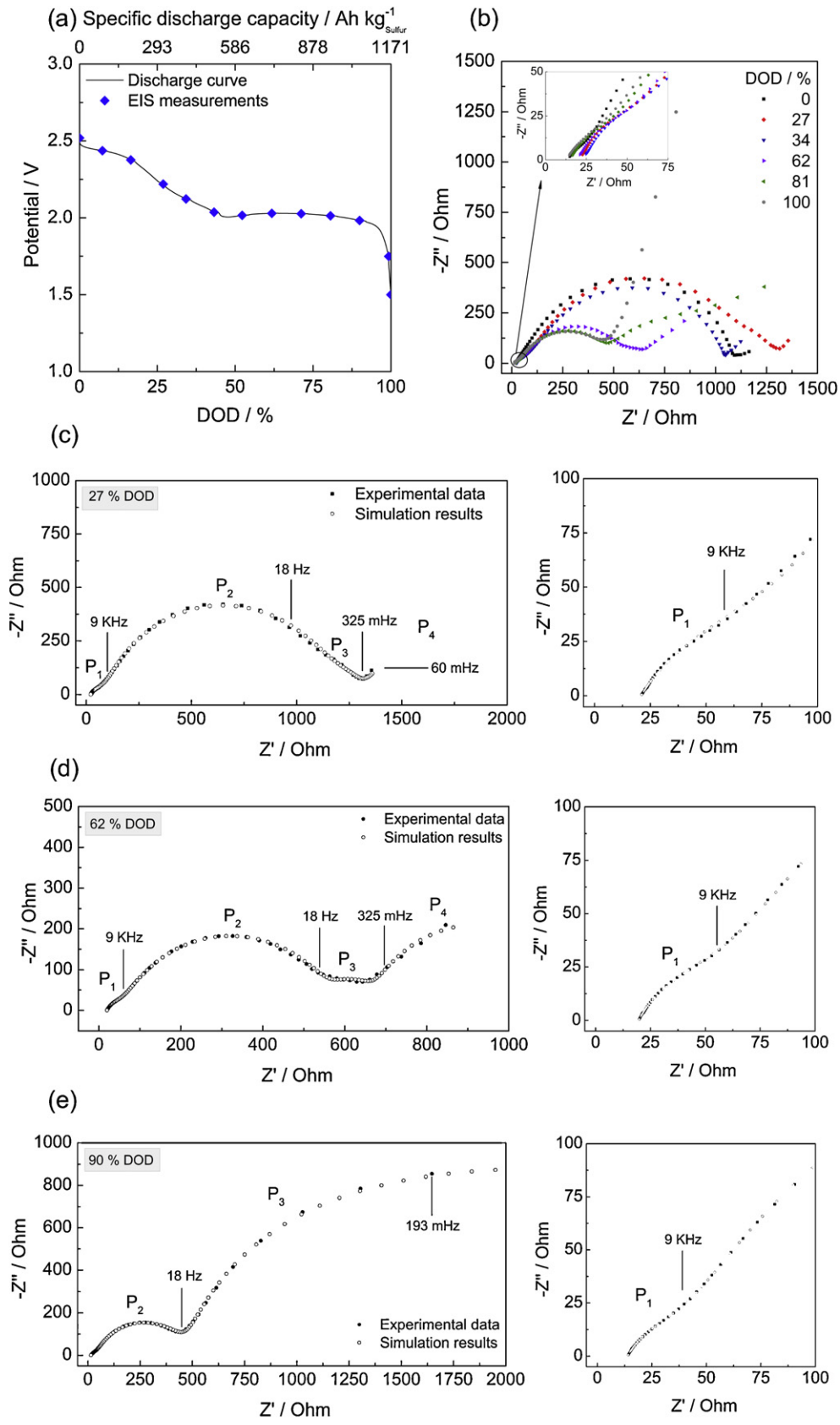

Fig. 2. (a) Discharge curve of a Li–S battery; each point represents an EIS measurement. (b) Selected Nyquist plots in the frequency range of 60 mHz–1 MHz at different depths of discharge, DOD. Experimental and fitting results of the EIS measurements at 27%, 62% and 90% DOD are shown in (c), (d) and (e), respectively. The high frequency regions of the spectra are amplified on the right.

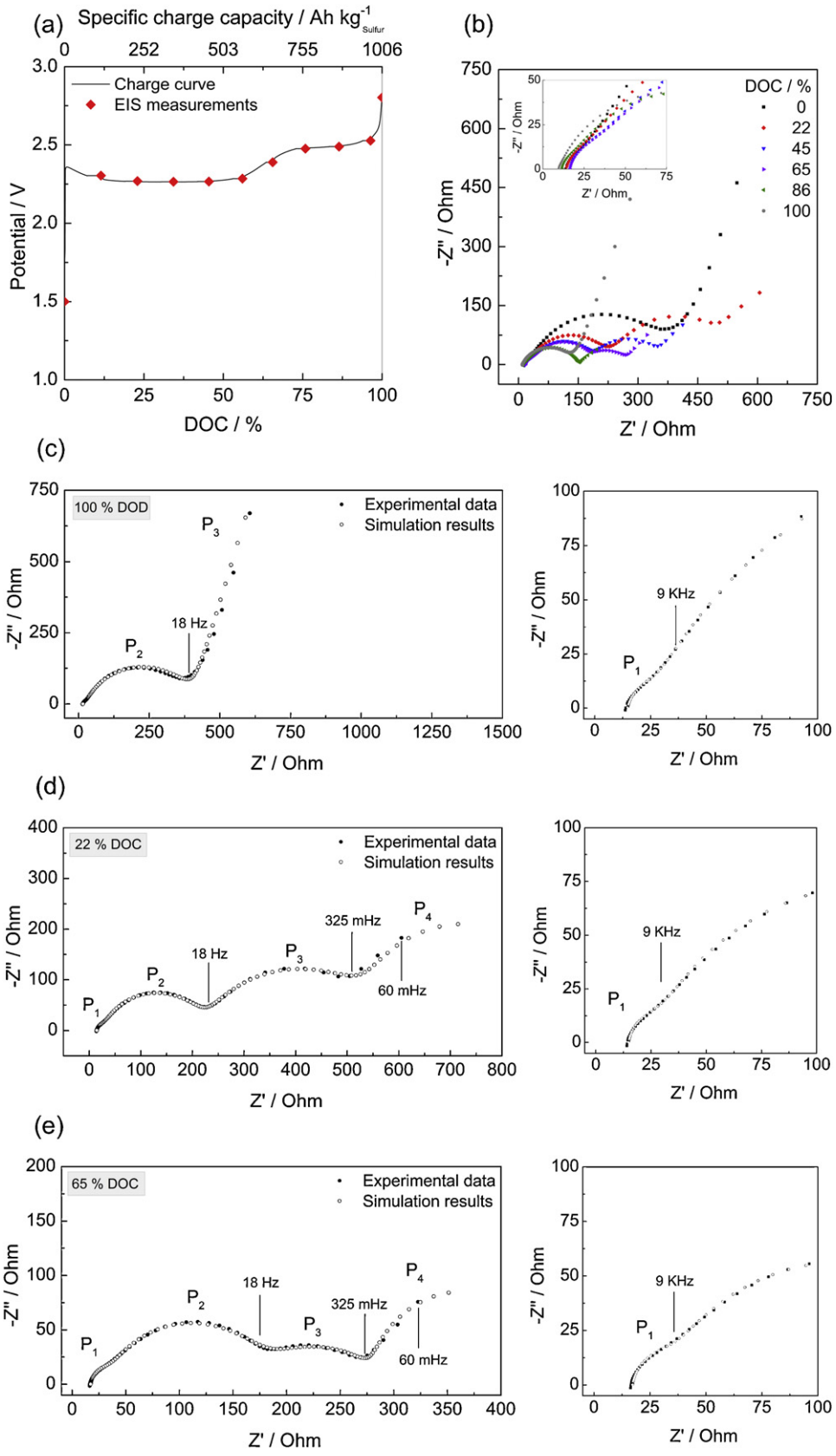

Fig. 3. (a) Charge curve of a Li–S battery; each point represents an EIS measurement. (b) Selected Nyquist plots in the frequency range of 60 mHz–1 MHz at different depths of discharge, DOD. Experimental and fitting results of the EIS measurements at 100% DOD, 22% DOC and 65% DOC are shown in (c), (d) and (e), respectively. The high frequency regions of the spectra are amplified on the right.

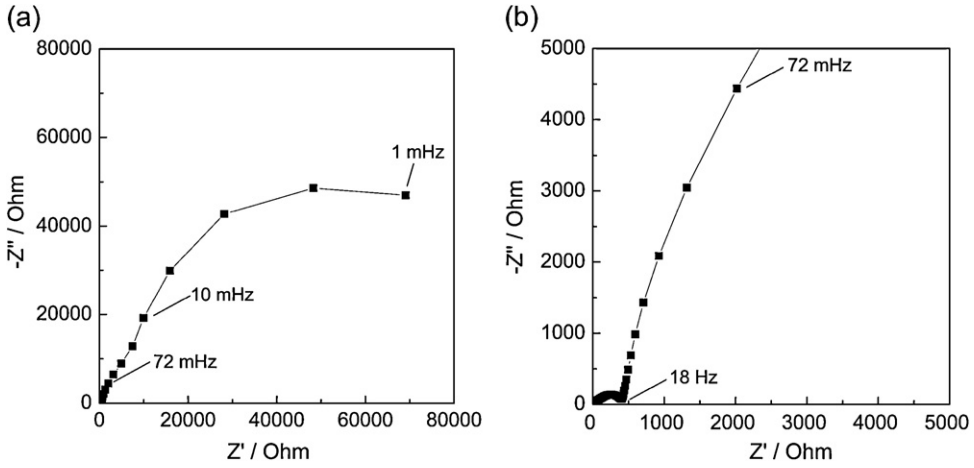

Fig. 4. Nyquist plot of a Li–S battery, frequency range: 1 mHz–1 MHz (a) with magnification in the frequency range: 72 mHz–1 MHz (b).

the form of two or three depressed semicircles. The number of semicircles that appear in the spectra is dependent on the DOD/DOC. At low frequencies, a distinct additional process is observed, which is shown by a bended slope line. To correlate this last process with a proper element of an EC, the spectrum was expanded in the lower frequency range down to 1 mHz (Fig. 4). This measurement reveals that processes at low frequencies also take the form of a semicircle. No inductance is observed in the EIS spectra at high frequencies.

At high frequencies, a semicircle with a relatively small diameter (low resistance) can be observed during discharging. We named this process P_1 and found that it is present in all EIS measurements and can be seen, for example, in a magnified image in Fig. 2(c and d). In the middle frequency range, a larger depressed semicircle is observed (P_2) during cycling. This larger semicircle is accompanied by a short bended line at low frequencies (P_4). From a 16% depth of discharge (DOD), a new semicircle (P_3) appears between P_2 and P_4. P_3 vanishes after 27% of DOD (Fig. 2(c)) and reappears at approximately 50% DOD, growing continuously, like it can be seen in Fig. 2(d and e), until the end of discharge. At higher states of discharge, P_3 becomes more significant, whereas P_4 (at low frequencies) is suppressed (see Fig. 2(e)).

During charging (Fig. 3), the processes P_1–P_4 can also be discerned. P_1 is present during charging in the high frequency range and semicircle P_2 decreases with increasing DOC. The semicircle corresponding to P_3 diminishes continuously with an increasing depth of charge (DOC) (compare loop P_3 in Fig. 3(d) and (e)). At the end of charge, a small increase is observed (see modeling results). Finally, the process P_4 behaves concurrently with P_3.

The processes P_1–P_4 are observed at different cutoff frequencies in the MHz-, kHz-, Hz- and mHz-domains, respectively.

3.2. Equivalent circuit for Li–S batteries

An equivalent electrical circuit consisting of an ohmic resistance R_0 in series with four R//CPE elements (R and CPE connected in parallel) was designed to model the EIS results (Fig. 5(a)). A CPE was selected instead of a capacitor because of the non-ideal behavior of the system, reflected as depressed semicircles in the Nyquist plots. In the low frequency region, neither a Warburg element nor a capacitive element could be identified (Fig. 4).

A CPE is similar to an ideal capacitive element, but has an absolute phase angle of less than 90°. The CPE impedance is defined as $Z = 1/(\omega_0 V(j\omega/\omega_0))^{\alpha}$, where ω is the angular frequency, ω_0 is a normalization factor, and V and α are constants [26]. The variable α is dimensionless ($\alpha \leq 1$) and defines the grade of compression of the CPE semicircle. The limit value of $\alpha = 1$ represents ideal capacitive behavior. In our measurements, α varies between 0.48 and 1.

Depressed semicircles such as P_3, could be the result of the superposition of many semicircles, as several parallel reactions occur in the battery. Nevertheless, these depressed semicircles

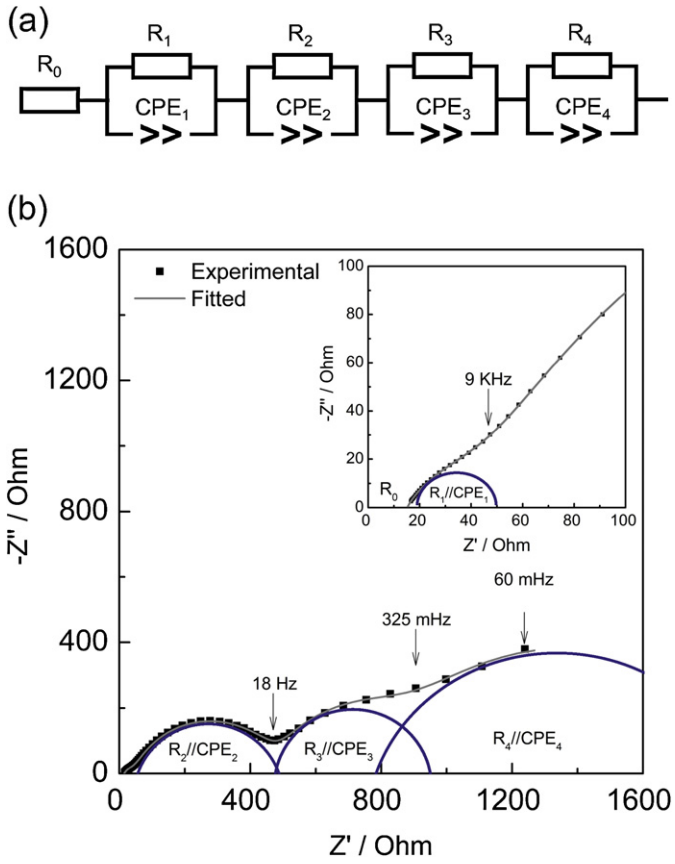

Fig. 5. (a) Equivalent electrical circuit of a Li–S battery used to fit the experimental data. (b) Nyquist plot of the impedance response of the battery at 81% DOD. The blue semicircles are schematics to clarify the domain of each EC element. The high frequency region of the spectrum is magnified at the top. (For interpretation of the references to color in this figure legend, the reader is referred to the web version of the article.)

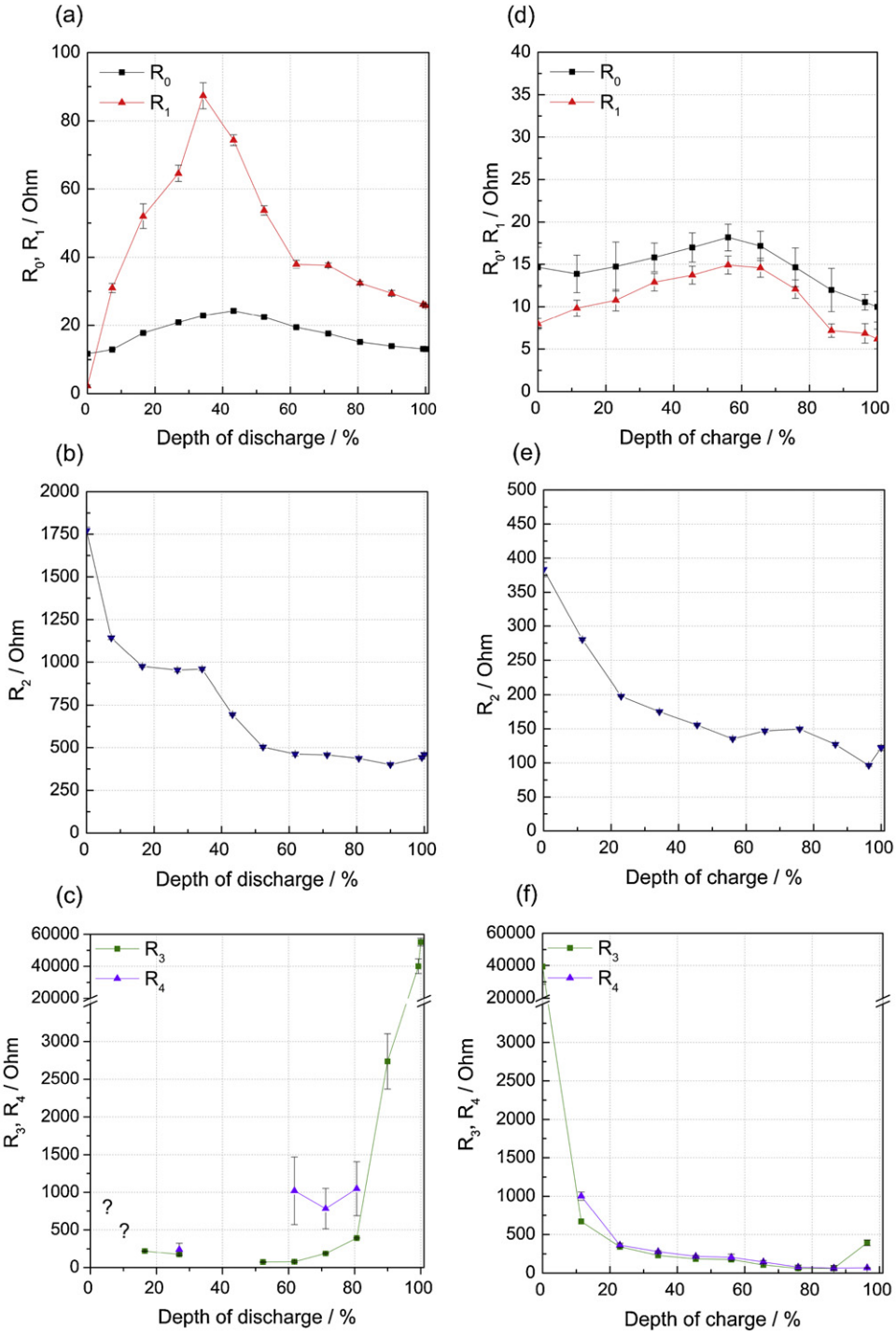

Fig. 6. Charge transfer resistances calculated by modeling the impedance spectra measured during the first discharge (a–c) and charge (d–f) of the Li–S battery at DOD/DOC.

cannot be identified separately and the EC must be simplified in one depressed semicircle. Non-ideal behavior can also be explained by inhomogeneities of the electrode material, roughness and gradient concentrations.

In Fig. 5(b), an example of an EIS spectrum at 81% DOD and its fitting to the EC of Fig. 5(a) is shown. The blue semicircles in the image are only guides to the eye. As shown, the experimental points fitted well with the equivalent circuit. The different processes described previously (P_1–P_4) are now described by the corresponding R//CPE elements of the EC. Depending on the depth of charge or discharge, R_3//CPE_3 and/or R_4//CPE_3 may not be present or may be indistinguishable in the frequency range of measurement.

R_0 represents the ohmic resistance contribution resulting from the electrolyte resistance, current collectors and cell connections. Changes observed in R_0 are normally associated with variations in electrolyte properties such as chemical composition or viscosity. The electrolyte in Li–S batteries is considerably affected during cycling, because solid reaction products dissolve partially (like sulfur) and soluble polysulfides, Li_2S_x (with $x = 3$–8), are accumulated during charging and discharging. The dissolution of polysulfides increases the viscosity of the electrolyte and the resistance.

The first loop at high frequency, R_1//CPE_1, may be associated with the charge transfer occurring at the anode surface. This interpretation is based on analysis of the simulation results in Fig. 6. First, the clear, concurrent behavior of R_0 and R_1 as a function of DOD or DOC is observed. This implies that P_1 is also affected by the concentration of polysulfides that can be reduced at the anode, which leads to charge transfer inhibition. Second, the resistance values of P_1 are much lower than those of P_2 (related to the charge transfer resistance of the cathode, see explanation below). This lower resistance of P_1 is related to the lower surface area of the anode compared to the cathode.

The R_2//CPE_2 element is attributable to the charge transfer of sulfur intermediates, and R_3//CPE_3 is attributable to the formation and dissolution of S_8 and Li_2S. The correlation of these EC-elements with specific chemical processes occurring in the battery was conceived after analysis of the simulation results. Note that R_2 is highest at 0% discharge where the concentration of sulfur intermediate is minimized. On the contrary, R_3 obtains its highest value at full discharge where accessible S_8 is unavailable and obtains its lowest values after sulfur disolution. R_3 is visible when the formation of Li_2S starts. Both the electrochemical reactions and the resistance of each EC-element exhibit a distinct DOD/DOC dependence. This result and a comparison with other characterization techniques such as XRD and AFM [23,25], along with results from the previous literature [19–22], support our assignment of the elements in the EC.

Finally, diffusion processes are detected by means of EIS at low frequencies. In our circuit, these processes are simulated by the element R_4//CPE_4.

3.3. Modeling of EIS during the first cycle

The circuit elements (ohmic resistance, charge transfer resistances and associated double layer capacitance) were calculated by fitting the experimental data points with the EC. The complete results of the fitting are presented in the supplemental information. The resistance contributions as functions of DOD and DOC for the first cycle are illustrated in Fig. 6. The electrolyte resistance (R_0) changes during discharge and is influenced by the concentration of soluble polysulfides (Fig. 6(a)). High resistances are measured from 34 to 52% DOD, indicating states with maximal concentrations of polysulfides corresponding to the end of the first plateau in the discharge curve. When the reduction of polysulfides to dilithium sulfide is complete, R_0 reduces back to approximately its original values. The charge transfer resistance in the anode, R_1, shows a trajectory similar to but more pronounced than that of R_0, with a maximum at 34% DOD. The electrolyte has a high concentration of dissolved polysulfides, which can diffuse to the anode surface and hinder the charge transfer of lithium ions.

The charge transfer resistance on the cathode side, described by R_2, decreases during discharge (Fig. 6(b)). The drastic diminution of resistance R_2 during the first stages of discharge may be caused by the changes in composition and morphology occurring in the cathode during this period. As a consequence of the dissolution and reaction of sulfur, the content of solid sulfur in the cathode diminishes; a more porous structure remains, with a higher surface area and greater conductivity. The charge transfer of polysulfide ions is enhanced as a result of these factors. In the interval between 16% and 34% DOD, the resistance remains constant. At this stage, process P_3 can be recognized at 16% and 27% DOD (see fitting curve in Fig. 2(c)). The reason for the appearance of process P_3 may be the slowing of an electrochemical step, which is seen as a new CPE element in the spectrum. The presence of this element at the first stages of discharge is related to the dissolution of the remaining sulfur in the cathode. The dissolution and progressive reaction of sulfur was monitored by means of in situ XRD in [24]. At 0% DOD, a small loop associated with P_3 can be observed between P_2 and P_4. Nevertheless, the small quantity of measured points result in an imprecise quantification, and we decided to model the spectrum of the completely charged battery (0% DOD) with three R//CPEs. After sulfur dissolves and reacts, P_3 cannot be observed until 52% DOD is reached. The reappearance of this process at this discharge state is now attributable to the formation of Li_2S. The resistance of this element increases continuously until the end of discharge, due to the gradual formation of this solid and low electrically conductive end product of the Li–S discharge reaction (Fig. 6(c)). Moreover, R_2 stabilizes at the final stages of discharge with the progressive reduction of polysulfides.

R_4, which is attributed to diffusion, could not always be determined as a result of an insufficient number of measured points at low frequencies. However, it could be observed that R_4 follows the tendency of P_3 (Fig. 6(c)). The dissolution or formation of solid isolating materials can influence the diffusion of species, negatively in the case of solid products formation. Diffusion is suppressed by the dominant process P_3 at values higher than 81% DOD, and it is displaced out of the measured frequency range. This can be clearly observed in Fig. 2(e), at 90% DOD, where the large P_3 semi-circle is present in the low frequency range.

During the charge step (Fig. 6(d–f)), an overall decrease in the absolute values of the resistance elements is observed in comparison with the discharge step. The maximum values of R_0 and R_1 occur at approximately 60% DOC. In contrast to the discharge process, the maximum concentration of polysulfides in the electrolyte occurs in the second half of the charging process, at the end of the first plateau. At this point, dilithium sulfide has been completely reacted to high order polysulfides.

The resistance related to the charge transfer in the cathode, R_2, decreases and stabilizes after approximately 40% DOC. The most important changes in the cathode morphology may occur during the first discharge, when the sulfur particles dissolve and leave the cathode. Afterwards, the formation of solid products may occur primarily at the surface of the cathode. For this reason, the charge transfer of the cathode during the first charge does not induce such pronounced changes as it does during the first discharge.

The reaction of Li_2S in the first stages of charging enhances the diminution of R_3 considerably. The most drastic changes in R_3 occur

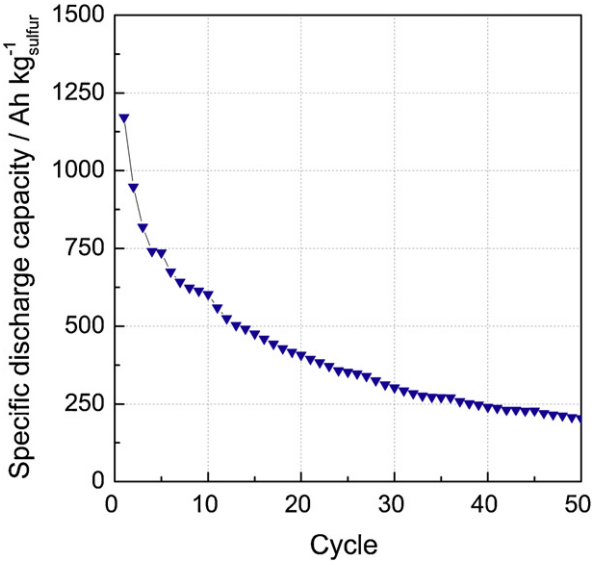

Fig. 7. Cycle performance of a Li–S battery at room temperature for up to 50 cycles.

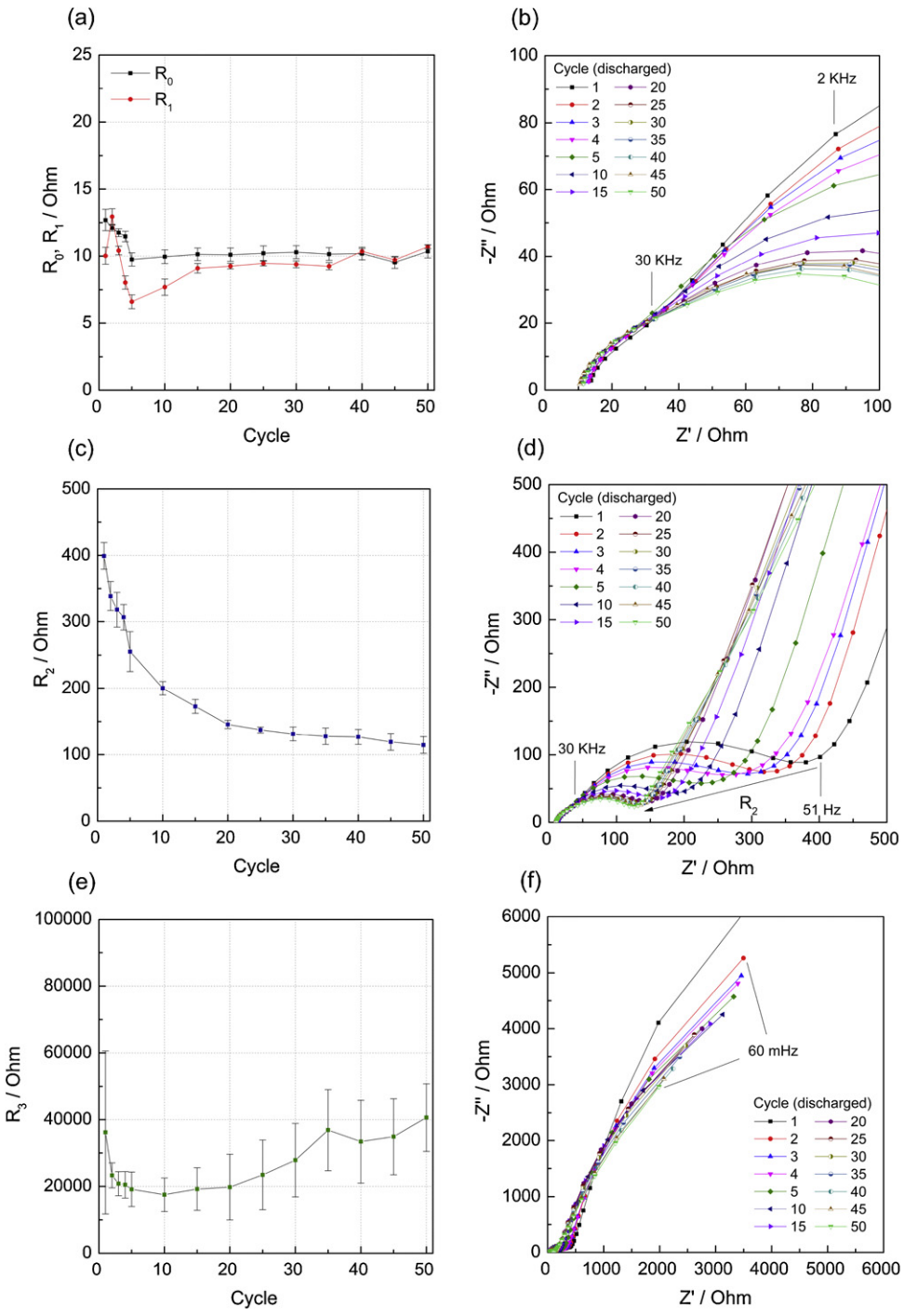

Fig. 8. Charge transfer resistances calculated by modeling the impedance spectra measured in a discharge state for up to 50 cycles (a, c, and e). Selected impedance spectra are shown for each frequency domain (b, d, and f).

in the period between 100% DOD and 22% DOC (Fig. 6 (f)). This can be observed in Fig. 3(c and d). At the end of the charging cycle, an increase in R_3 is observed due the formation of solid S_8. The resistance related to diffusion (R_4) can be clearly linked to the dissolution of Li_2S and the formation of sulfur, with both following the same trajectory.

3.4. Degradation during cycling

The degradation of the battery over 50 cycles was investigated by means of EIS. The cycle performance of the battery is shown in Fig. 7. The specific discharge capacity of the cell is high at the beginning of the cycling (approximately 1200 mAh g^{-1}), but the battery degrades with an increasing number of cycles. Some degradation of the cell is due to the aging of the battery during testing. Although the cathode used does not present the highest constant capacity, it is still important to characterize the degradation and fading of the capacity of this cell to understand potential modifications and improvements. This simple but industrially viable cathode can be improved, for example, by the use of protective layers and electrolyte additives, as was experimentally proven in [27–32].

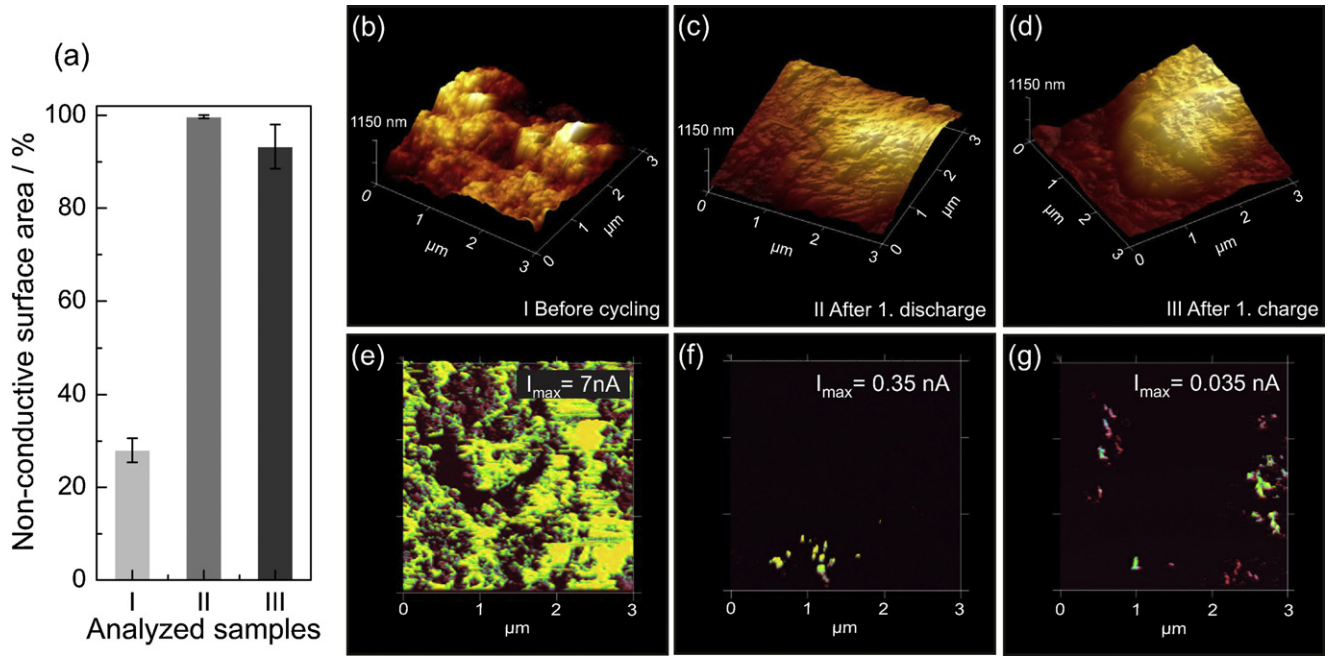

Fig. 9. (a) Non-conductive surface area (%) for the analyzed samples where I: cathode before cycling, II: cathode surface after the first discharge and III: cathode surface after the first charge. (b–d) AFM topography images of the samples. (e and f) AFM current images.

The results of fitting the battery in a discharge state with the impedance spectra are summarized in Fig. 8. In the high frequency region, the low ohmic resistance R_0 and charge transfer resistance R_1 do not change appreciably with an increased number of cycles (Fig. 8(a and b)).

The resistance associated with the charge transfer of the cathode (R_2), measured in the discharge state, decreases drastically in the first few cycles, decreasing 50% between the 1st and 10th cycles (Fig. 8(c)). The rate of loss of resistance is similar to the rate of the fading of capacity (49%). The battery loses 83% of its specific discharge capacity in 50 cycles, while the major decrease (49%) occurs in the first 10 cycles. From the 10th to the 20th cycle, a more gradual diminution is observed. The loss of discharge capacity behaves concurrently with the diminution of charge transfer resistance in the cathode. The high reduction of R_2 is most likely associated with the better accessibility of active material by electronic conduction; related to the less formation of non-conductive Li_2S. The charge transfer resistance in the cathode reduces; however, the degradation of the cell increases, resulting in lower discharge capacities.

The resistance R_3 cannot be precisely fitted in the same manner as the other circuit elements (Fig. 8(e)). Evaluation of this element shows larger errors due to the fewer available measurement points at low frequencies. The formation of Li_2S, which is linked to this element, decreases during cycling. This decrease is reflected by the reduction of the resistance at the beginning of the cycle. Nevertheless, the resistance increases gradually after 10 cycles. This may be a result of a gradual degradation of the cathode due to the growth of an isolated film at the boundary between cathode and separator, composed of solid reaction products. On the contrary, the bulk of the cathode may consist, at the end of the 50th cycle, essentially of carbon black and some isolated sulfur particles. The concentration of non-conductive reaction products may increase in the direction of the surface of the cathode. This can be explained by the reduction of charge transfer resistance related to the reaction of soluble polysulfides, R_2, and the high resistance R_3 due to the formation of a non-conductive layer on the surface.

3.5. AFM measurements

The electrical conductivity of the cathode was evaluated by means of conductive AFM. The measured current, directly proportional to the electrical conductivity of the path between the sample surface and the sample holder, is influenced by the composition of the sample (percentage of non-conductive material), the homogeneity of the sample, the distribution of non-conductive particles in the bulk material and the formation of non-conductive surface layers. If an isolating surface layer is present, no current can be measured and the non-conductive area can be quantified.

Each sample was analyzed in three different positions over a scan area of 3 µm × 3 µm. The results of the non-conductive surface area quantification, the AFM images of the topography of the cathode and the current distribution are shown in Fig. 9. Before cycling, the cathode has a homogeneous surface covered mainly with carbon black (28% of the non-conductive surface area). After the first discharge, the sample is covered with an isolating film, which reduces the conductive area to less than 1% of the total area. The film is accumulated during the last period of discharge and consists mainly of non-conductive Li_2S. This explains the radical increase of R_3 at the end of the cycle. In air, Li_2S reacts to LiOH, which is also a non-conductive material but is stable under ex situ conditions. After charging, the cathode has a high percentage of non-conductive area (93%) with inhomogeneities in the surface. Similar tendencies toward conductivity changes on cathode surfaces were also reported from in situ AFM measurements in previous studies [33].

The AFM results confirm the formation of an isolating layer in the cathode, which increases the surface resistance on the cathode, as observed through the analysis of the impedance at low frequencies (R_3).

4. Conclusions

In this work, a Li–S battery was investigated by means of EIS. An equivalent circuit is proposed for the evaluation of Li–S

batteries, which can be applied in a broad frequency domain. The elements of this circuit have been related to physical and chemical processes occurring in the anode, cathode and electrolyte. The impedance contributions associated with these processes are strongly dependent on the depths of discharge and charge of the cell. During the first cycle, the dissolution and formation of solid reaction products can be detected and evaluated through the appearance of an additional semicircle in the middle frequency region of the Nyquist impedance plot. The highest electrolyte resistance, related to the highest concentration of polysulfides, is detected at 43% DOD and 56% DOC, at the end of the first discharge and charge plateau, respectively. The study of the degradation of the cathode by means of EIS for up to 50 cycles shows that the impedance contributions related to the electrolyte and the anode side present only small changes, while the charge transfer resistance in the cathode is reduced by 71%. This diminution may be related to the rate capacity loss of the battery as a result of the lessened formation of non-conductive solid products in the cathode bulk. AFM measurements confirm the formation of a solid isolating layer after cycling, in discharge and charge states.

Acknowledgments

The authors wish to acknowledge financial support for instrumentation from the Federal Ministry of Education and Research within the project “Elektrochemie für Elektromobilität – Verbund Süd -03KP801” and from the State Ministry for Research and Education of Baden-Württemberg.

The authors also wish to thank Alexander Bauder for his support in modeling the EIS spectra and Christian Hellwig for an enriching discussion on EIS measurement interpretation.

Appendix A. Supplementary data

Supplementary data associated with this article can be found, in the online version, at http://dx.doi.org/10.1016/j.electacta.2013.02.101.

References

[1] Y.V. Mikhaylik, J.R. Akridge, Polysulfide Shuttle Study in the Li/S Battery System, Journal of the Electrochemical Society 151 (2004) A1969.
[2] V.S. Kolosnitsyn, E.V. Karaseva, Electrochemistry of a lithium electrode in lithium polysulfide solutions, Russian Journal of Electrochemistry 44 (2008) 506.
[3] J. Akridge, Li/S fundamental chemistry and application to high-performance rechargeable batteries, Solid State Ionics 175 (2004) 243.
[4] Y.M. Lee, N.-S. Choi, J.H. Park, J.-K. Park, Electrochemical performance of lithium/sulfur batteries with protected Li anodes, Journal of Power Sources 119–121 (2003) 964.
[5] J. Hassoun, M. Agostini, A. Latini, S. Panero, Y.-K. Sun, B. Scrosati, Nickel-Layer Protected, Carbon-Coated Sulfur Electrode for Lithium Battery, Journal of the Electrochemical Society 159 (2012) A390.
[6] Y.-J. Choi, Y.-D. Chung, C.-Y. Baek, K.-W. Kim, H.-J. Ahn, J.-H. Ahn, Effects of carbon coating on the electrochemical properties of sulfur cathode for lithium/sulfur cell, Journal of Power Sources 184 (2008) 548.
[7] J. Ma, A. Manthiram, Orthorhombic Bipyramidal Sulfur Coated with Polypyrrole Nanolayers As a Cathode Material for Lithium–Sulfur Batteries, Journal of Physical Chemistry 116 (2012) 8910.
[8] J. Wang, J. Chen, K. Konstantinov, L. Zhao, S.H. Ng, G.X. Wang, Z.P. Guo, H.K. Liu, Sulphur-polypyrrole composite positive electrode materials for rechargeable lithium batteries, Electrochimica Acta 51 (2006) 4634.
[9] J. Sun, Y. Huang, W. Wang, Z. Yu, A. Wang, K. Yuan, Preparation and electrochemical characterization of the porous sulfur cathode using a gelatin binder, Electrochemistry Communications 10 (2008) 930.
[10] F. Zhang, Y. Dong, Y. Huang, G. Huang, X. Zhang, L. Wang, Preparation and performance of a sulfur/graphene composite for rechargeable lithium-sulfur battery, Journal of Physics: Conference Series 339 (2012) 012003.
[11] B. Zhang, C. Lai, Z. Zhou, X.P. Gao, Preparation and electrochemical properties of sulfur–acetylene black composites as cathode materials, Electrochimica Acta 54 (2009) 3708.
[12] Y.-S. Su, A. Manthiram, A facile in situ sulfur deposition route to obtain carbon-wrapped sulfur composite cathodes for lithium–sulfur batteries, Electrochimica Acta 77 (2012) 272.
[13] N.-I. Kim, C.-B. Lee, J.-M. Seo, W.-J. Lee, Y.-B. Roh, Correlation between positive-electrode morphology and sulfur utilization in lithium–sulfur battery, Journal of Power Sources 132 (2004) 209.
[14] D. Aurbach, K. Gamolsky, B. Markovsky, Y. Gofer, M. Schmidt, U. Heider, On the use of vinylene carbonate (VC) as an additive to electrolyte solutions for Li-ion batteries, Electrochimica Acta 47 (2002) 1423.
[15] W. Wang, Y. Wang, Y. Huang, C. Huang, Z. Yu, H. Zhang, A. Wang, K. Yuan, The electrochemical performance of lithium–sulfur batteries with $LiClO_4$ DOL/DME electrolyte, Journal of Applied Electrochemistry 40 (2009) 321.
[16] B. Jin, J.-U. Kim, H.-B. Gu, Electrochemical properties of lithium–sulfur batteries, Journal of Power Sources 117 (2003) 148.
[17] H.-S. Ryu, H.-J. Ahn, K.-W. Kim, J.-H. Ahn, K.-K. Cho, T.-H. Nam, J.-U. Kim, G.-B. Cho, Discharge behavior of lithium/sulfur cell with TEGDME based electrolyte at low temperature, Journal of Power Sources 163 (2006) 201.
[18] X. Liang, Z. Wen, Y. Liu, M. Wu, J. Jin, H. Zhang, X. Wu, Improved cycling performances of lithium sulfur batteries with $LiNO_3$-modified electrolyte, Journal of Power Sources 196 (2011) 9839.
[19] L. Yuan, X. Qiu, L. Chen, W. Zhu, New insight into the discharge process of sulfur cathode by electrochemical impedance spectroscopy, Journal of Power Sources 189 (2009) 127.
[20] Y. Li, H. Zhan, S. Liu, K. Huang, Y. Zhou, Electrochemical properties of the soluble reduction products in rechargeable Li/S battery, Journal of Power Sources 195 (2010) 2945.
[21] V.S. Kolosnitsyn, E.V. Kuz'mina, E.V. Karaseva, S.E. Mochalov, Impedance spectroscopy studies of changes in the properties of lithium-sulfur cells in the course of cycling, Russian Journal of Electrochemistry 47 (2011) 793.
[22] C. Barchasz, J.-C. Leprêtre, F. Alloin, S. Patoux, New insights into the limiting parameters of the Li/S rechargeable cell, Journal of Power Sources 199 (2012) 322.
[23] N.A. Cañas, S. Wolf, N. Wagner, K.A. Friedrich, In-situ X-ray diffraction studies of lithium-sulfur batteries, Journal of Power Sources 226 (2013) 313.
[24] R. Hiesgen, S. Helmly, I. Galm, T. Morawietz, M. Handl, K. Friedrich, Microscopic Analysis of Current and Mechanical Properties of Nafion® Studied by Atomic Force Microscopy, Membranes 2 (2012) 783.
[25] C. Barchasz, F. Molton, C. Duboc, J.-C. Leprêtre, S. Patoux, F. Alloin, Lithium/sulfur cell discharge mechanism: an original approach for intermediate species identification, Analytical Chemistry 84 (2012) 3973.
[26] SIM Manual Zahner® (04/2012). Available at: http://www.zahner.de/pdf/SIM.pdf (accessed: 04.12.12).
[27] H. Schneider, A. Garsuch, A. Panchenko, O. Gronwald, N. Janssen, P. Novák, Influence of different electrode compositions and binder materials on the performance of lithium – sulfur batteries, Journal of Power Sources 205 (2012) 420.
[28] G.-C. Li, G.-R. Li, S.-H. Ye, X.-P. Gao, A Polyaniline-Coated Sulfur/Carbon Composite with an Enhanced High-Rate Capability as a Cathode Material for Lithium/Sulfur Batteries, Advanced Energy Materials 2 (2012) 1238.
[29] Y.-S. Su, A. Manthiram, Lithium–sulphur batteries with a microporous carbon paper as a bifunctional interlayer, Nature Communications 3 (2012) 1166.
[30] Z. Lin, Z. Liu, W. Fu, N.J. Dudney, C. Liang, Phosphorous Pentasulfide as a Novel Additive for High-Performance Lithium-Sulfur Batteries Advanced, Advanced Functional Materials 23 (2013) 1064.
[31] S. Xiong, K. Xie, Y. Diao, X. Hong, Properties of surface film on lithium anode with $LiNO_3$ as lithium salt in electrolyte solution for lithium–sulfur batteries, Electrochimica Acta 83 (2012) 78.
[32] W. Chen, Q. Li, Y. Chen, P. Dai, Z. Jiang, The Enhanced Electrochemical Performance of Lithium/Sulfur Battery with Protected Lithium Anode, Advanced Materials Research 476-478 (2012) 676.
[33] R. Elazari, G. Salitra, Y. Talyosef, J. Grinblat, C. Scordilis-Kelley, A. Xiao, J. Affinito, D. Aurbach, Morphological and Structural Studies of Composite Sulfur Electrodes upon Cycling by HRTEM, AFM and Raman Spectroscopy, Journal of the Electrochemical Society 157 (2010) A1131.